Monthly Notices
of the
ROYAL ASTRONOMICAL SOCIETY

MNRAS **505,** 5543–5553 (2021)
Advance Access publication 2021 June 11

https://doi.org/10.1093/mnras/stab1674

High [O III]/[C II] surface brightness ratios trace early starburst galaxies

L. Vallini ,★ A. Ferrara, A. Pallottini , S. Carniani and S. Gallerani

Scuola Normale Superiore, Piazza dei Cavalieri 7, I-56126 Pisa, Italy

Accepted 2021 June 8. Received 2021 June 7; in original form 2021 March 12

ABSTRACT

We study the impact of deviations from the Kennicutt–Schmidt relation (quantified by the 'burstiness' parameter κ_s), gas metallicity (Z), and density (n) on the observed [O III]88 μm/[C II]158 μm surface brightness ratios ($\Sigma_{[O\,III]}/\Sigma_{[C\,II]}$) in nine galaxies at $z \approx 6-9$. We first discuss possible biases in the measured $\Sigma_{[O\,III]}/\Sigma_{[C\,II]}$ ratios by comparing the data with zoom-in cosmological simulations and then use a Markov Chain Monte Carlo algorithm to derive the best-fitting values of (κ_s, Z, n). We find that (i) the strongest dependence of $\Sigma_{[O\,III]}/\Sigma_{[C\,II]}$ is on κ_s; (ii) high ratios identify starburst galaxies with short gas depletion times ($t_{dep} = 6 - 49$ Myr); (iii) a secondary dependence on density is found, with $\Sigma_{[O\,III]}/\Sigma_{[C\,II]}$ anticorrelating with n as a result of the lower [O III] critical density; and (iv) the ratio weakly depends only on Z. The nine galaxies are significantly enriched ($Z = 0.2-0.5\,Z_\odot$) and dense $n \approx 10^{1-3}$ cm^{-3}. This lends further support to the starburst scenario in which a rapid enrichment of the interstellar medium is expected.

Key words: ISM: evolution – ISM: photodissociation region – galaxies: high-redshift – galaxies: ISM – galaxies: starburst.

1 INTRODUCTION

The Atacama Large Millimeter Array (ALMA; Carilli & Walter 2013) opened a window on the characterization of the interstellar medium (ISM), star formation, and chemical enrichment in the Epoch of Reionization (EoR) as traced by far-infrared (FIR) lines. Among FIR lines, the fine-structure $^2P_{3/2} \rightarrow {}^2P_{1/2}$ transition of the ionized carbon ([C II]) at 158 μm is one of the most luminous (Stacey et al. 1991), with the [C II] line mostly tracing the cold neutral diffuse gas (Wolfire et al. 2003) and the dense photodissociation regions (PDRs; Hollenbach & Tielens 1999) associated with molecular clouds. After the first, pioneering, detections in galaxies at $z > 5.5$ (Capak et al. 2015; Maiolino et al. 2015), [C II] has now been observed and often spatially resolved in ≈100 galaxies at $4 < z < 5.5$ (ALPINE-Survey; Béthermin et al. 2020; Le Fèvre et al. 2020) and in tens of $z = 6-8$ sources (Willott et al. 2015; Knudsen et al. 2016; Pentericci et al. 2016; Bradač et al. 2017; Matthee et al. 2017; Carniani et al. 2018a,b; Smit et al. 2018; Fujimoto et al. 2019; Hashimoto et al. 2019; Matthee et al. 2019; Bakx et al. 2020; Calura et al. 2021; Herrera-Camus et al. 2021). In addition to [C II], ALMA has been also exploited to target EoR sources via the $^3P_1 \rightarrow {}^3P_0$ transition of doubly ionized oxygen ([O III]) at 88 μm (Inoue et al. 2016; Carniani et al. 2017; Laporte et al. 2017a; Hashimoto et al. 2019; Tamura et al. 2019; Carniani et al. 2020; Harikane et al. 2020).

Joint [C II]–[O III] line detections have a huge diagnostic potential as they yield complementary views of the ISM at early epochs. While [O III] traces ionized gas in H II regions (Cormier et al. 2015), [C II] mainly arises from neutral/molecular gas. Notably, the [O III]/[C II] luminosity ratios ($L_{[O\,III]}/L_{[C\,II]}$) in galaxies at $7 < z < 9$ (Inoue et al. 2016; Hashimoto et al. 2019; Carniani et al. 2020; Harikane et al. 2020) exceed the highest values observed in local dwarf galaxies (Madden et al. 2013; Cormier et al. 2015), which are known to be bright [O III] emitters.

An increasing number of theoretical works (Vallini et al. 2013, 2015; Katz et al. 2017; Olsen et al. 2017; Pallottini et al. 2017; Lagache, Cousin & Chatzikos 2018; Kohandel et al. 2019; Pallottini et al. 2019; Arata et al. 2020; Lupi et al. 2020) suggest that the prevailing physical conditions of the ISM were extreme (e.g. large densities, high turbulence, strong radiation fields) and common among early galaxies. These findings provide a solid basis to investigate the origin of the observed high $L_{[O\,III]}/L_{[C\,II]}$ ratios.

Possible explanations include high-ionization parameters (U) (Katz et al. 2017; Moriwaki et al. 2018; Pallottini et al. 2019), high filling factor of ionized gas versus gas in dense PDRs (Harikane et al. 2020), intermittent starbursting phases in the star formation histories of the EoR galaxies (Arata et al. 2020; Lupi et al. 2020), and photoevaporation feedback (Decataldo et al. 2017; Vallini et al. 2017). As outlined by Ferrara et al. (2019), all these conditions can be produced in the ISM of a starburst galaxy, hence located above the Kennicutt–Schmidt (KS) relation. As a matter of fact, a source with star formation rate surface density (Σ_{SFR}) exceeding the KS value at fixed gas surface density (Σ_{gas}) has a correspondingly larger U and therefore larger ionized gas column density as compared to a galaxy with the same Σ_{gas} but lying on the KS relation. These conditions boost (quench) ionized (neutral) gas tracers (Vallini et al. 2020).

Apart from gas ionization conditions, [C II] and [O III] line emission is also influenced by metallicity (Z): it has been shown that for $Z < 0.1\,Z_\odot$, the [C II] luminosity drops significantly (e.g. Vallini et al. 2015; Olsen et al. 2017; Pallottini et al. 2017; Lagache et al. 2018). At the same time, low-Z galaxies are expected to feature brighter [O III] luminosities (Cormier et al. 2015; Inoue et al. 2016; Vallini et al. 2017). Lower C/O ratios (Steidel et al. 2016; Arata et al. 2020), high densities (Harikane et al. 2020), and the compactness of EoR galaxies (Shibuya, Ouchi & Harikane 2015) can also partially explain large $L_{[O\,III]}/L_{[C\,II]}$ ratios.

★ E-mail: livia.vallini@sns.it

© 2021 The Author(s)
Published by Oxford University Press on behalf of Royal Astronomical Society

Downloaded from https://academic.oup.com/mnras/article/505/4/5543/6296656 by Scuola Normale Superiore Biblioteca user on 14 November 2022

However, the determination of $L_{[O\,III]}/L_{[C\,II]}$ ratios in early galaxies must be handled with caution. As noted by Carniani et al. (2020), the $L_{[O\,III]}/L_{[C\,II]}$ values of EoR sources are closer to those of local metal-poor dwarf galaxies when the [C II] flux loss is corrected for. The $L_{[O\,III]}/L_{[C\,II]}$ are in fact prone to overestimation because the [C II] emitting region of ALMA-detected galaxies at high-z is $\approx$2−3 times more extended (Carniani et al. 2018b; Fujimoto et al. 2019; Fujimoto et al. 2020; Ginolfi et al. 2020; Herrera-Camus et al. 2021) than the [O III]/rest-frame ultraviolet (UV) one. Flux losses due to the surface brightness dimming in [C II] can thus lead to a spurious underestimation of the actual [C II] luminosity (Kohandel et al. 2019).

Analysing instead the [O III]/[C II] surface brightness ratios ($\Sigma_{[O\,III]}/\Sigma_{[C\,II]}$) can overcome this problem as the different extension of the line emitting regions is explicitly accounted for when computing the line surface brightness. Additionally, the $\Sigma_{[O\,III]}/\Sigma_{[C\,II]}$ ratios, along with their relation with Σ_{SFR}, are more closely related to the *local* ISM conditions than the integrated $L_{[C\,II]}/L_{[O\,III]}$ ratios. For instance, the far-UV flux impinging upon PDRs – which is one of the fundamental parameters affecting the line surface brightness from PDR and ionized gas layers (e.g. Ferrara et al. 2019; Vallini et al. 2020) – is more tightly related to the local SFR surface density (e.g. Herrera-Camus et al. 2015; Díaz-Santos et al. 2017; Rybak et al. 2020; McKinney et al. 2021) than to the total galaxy SFR.

The aim of this work is precisely that of exploiting $\Sigma_{[O\,III]}/\Sigma_{[C\,II]}$ ratios with the goal of determining the star-forming and chemical enrichment conditions of the ISM in EoR galaxies, along with the physical mechanisms governing the [O III] and [C II] emission in early sources. To this aim, we build on the Ferrara et al. (2019) and Vallini et al. (2020) models that provide a physically motivated framework to compute the expected FIR line surface brightness tracing both ionized and neutral gas as a function of the deviation from the KS relation (κ_s), metallicity (Z), and gas density (n). The model also provides physically transparent interpretations of complex numerical simulations (Pallottini et al. 2019). The paper is organized as follows: in Section 2, we present the method and validate it on well-studied low-z sources; in Section 3, we apply the model to all the joint [C II]–[O III] detections in EoR so far available and compare the results with state-of-art cosmological zoom-in simulations. Section 4 discusses the implications of the results; our conclusions are given in Section 5.

2 METHOD

To study the physical mechanisms determining the $\Sigma_{[O\,III]}/\Sigma_{[C\,II]}$ ratios, we adopt the method presented in Vallini et al. (2020, V20 hereafter). In V20, the [C II] surface brightness ($\Sigma_{[C\,II]}$), the SFR surface density (Σ_{SFR}), and the surface brightness of a ionized gas tracer ($\Sigma_{line,ion}$) have been used to determine the (possible) deviation from the star formation law, the gas density, and metallicity of galaxies in the EoR. V20 focused on $\Sigma_{line,ion} = \Sigma_{C\,III]}$, i.e. the UV C III]λ1909 line, which is expected to be bright in the first galaxies (e.g. Stark et al. 2015). For the present analysis, we apply the model to the [O III]88 μm surface brightness ($\Sigma_{[O\,III]}$). In what follows, we summarize the rationale of the procedure, the fundamental equations, and their extension to oxygen lines.

2.1 Rationale, fundamental equations, and extension to [O III]

The V20 method is built upon the analytical model developed in Ferrara et al. (2019) that enables the computation of the line surface brightness from a gas slab with ionized/PDR column densities (N_{PDR}, N_i, respectively) determined by the average gas density (n) of the H II/PDR environment, the dust-to-gas ratio, ($\mathcal{D} \propto Z$), and ionization parameter, U. The latter can be expressed in terms of observed quantities by deriving its relation ($U \propto \Sigma_{SFR}/\Sigma_{gas}^2$, see equations 38 and 40 in Ferrara et al. 2019) with the star formation rate surface density (Σ_{SFR}) and the gas surface density (Σ_{gas}), which in turn are connected through the star formation law $\Sigma_{SFR} = \kappa_s \Sigma_{gas}^{1.4}$ (Kennicutt 1998). This leaves us with the κ_s parameter, describing the burstiness of the galaxy.

V20 adopted a Markov Chain Monte Carlo (MCMC) algorithm to search for the posterior probability of the best-fitting parameters (κ_s, Z, n) that reproduce the observed [C II] surface brightness ($\Sigma^{obs}_{[C\,II]}$, in $L_\odot$ kpc^{-2} units), C III]λ1909 surface brightness ($\Sigma^{obs}_{C\,III]}$, in $L_\odot$ kpc^{-2}), and the deviation ($\Delta^{obs}_{[C\,II]}$) from the local $\Sigma_{[C\,II]}$–Σ_{SFR} relation (De Looze et al. 2014):

$$\Sigma^{obs}_{[C\,II]} = F_{[C\,II]}(\kappa_s, Z, n) \quad (1)$$

$$\Sigma^{obs}_{C\,III]} = F_{C\,III]}(\kappa_s, Z, n) \quad (2)$$

$$\Delta^{obs}_{[C\,II]}(\Sigma^{obs}_{SFR}) = \Delta_{[C\,II]}(\kappa_s, Z, n). \quad (3)$$

In this work, instead of equation (2), we use $F_{[O\,III],88}(\kappa_s, Z, n)$, so that the input of the MCMC is the [O III] 88 μm surface brightness ($\Sigma^{obs}_{[O\,III]}$) instead of $\Sigma^{obs}_{C\,III]}$. To do so, we follow the same approach outlined in equation 29 and in appendix B of Ferrara et al. (2019). Adopting the same notation used in V20, the $F_{[O\,III],88}$ flux (in erg s^{-1} cm^{-2}) excited by collision with free electrons in a gas slab of density n and ionized hydrogen column-density $N_i(\kappa_s, Z)$ can be written as a function of the cooling rate ($\Lambda_{[O\,III],88}$) as:

$$F_{[O\,III],88} = n\Lambda_{[O\,III],88}\mathcal{A}_O Z N_i(\kappa_s, Z). \quad (4)$$

In the previous equation, the O^{2+} column density is approximated as $N_{O^{2+}} \approx \mathcal{A}_O Z N_i$ where we assume Asplund et al. (2009) abundance at solar metallicity ($\mathcal{A}_O \equiv$ O/H $= 4.89 \times 10^{-4}$ or $12 + \log$(O/H) $= 8.69$[1]). Moreover, we adopt a linear scaling with Z (which is in solar units).

The cooling rate ($\Lambda_{[O\,III],88} = n_1 A_{10} E_{10}$) follows from the computation of the population of the $^3P_1$ level. To derive the cooling rate as a function of temperature, T, and density n, we use Pyneb (Luridiana, Morisset & Shaw 2015). Such code solves the statistical equilibrium equation for the O^{2+} ion including all the possible transitions between the $^3P_0$, $^3P_1$, $^3P_2$, $^1D_2$, and $^1S_0$ levels:

$$\sum_{j\neq i} n n_j C_{ij}(T) + \sum_{j>i} n_j A_{ij} = \sum_{j\neq i} n_j n C_{ij}(T) + \sum_{j<i} n_i A_{ij}, \quad (5)$$

where C_{ij} are the collisional excitation (de-excitation) rate coefficients, A_{ij} are the Einstein coefficients for spontaneous emission, and $i = 0, .., 4$. The electron temperature in the ionized region is set to $T = 10^4$ K. This assumption is not very critical as the $^3P_1 \rightarrow {}^3P_0$ [O III]88 μm lines (and the other transition in the doublet, i.e. the $^3P_2 \rightarrow {}^3P_1$ transition at 52 μm) have similar excitation energy ($T_{ex,88} \approx 160$ K and $T_{ex,52} \approx 280$ K, respectively) but they have different critical densities $n_c \equiv A_{ij}/C_{ij}$. For this reason, the [O III]88 μm/[O III]52 μm ratio is not very sensitive to the gas temperature for $T > 1000\,K$ (Palay et al. 2012).

Equations (1), (4), (3), and the observed values and errors, $\Sigma^{obs}_{[C\,II]} \pm \delta_{[C\,II]}$, $\Sigma^{obs}_{[O\,III]} \pm \delta_{[O\,III]}$, $\Sigma^{obs}_{SFR} \pm \delta_{SFR}$ for each galaxy allow us to search for the posterior probability of the best-fitting parameters exploiting an MCMC algorithm. As in V20, we use the open-source EMCEE PYTHON implementation (Foreman-Mackey et al. 2013) of

[1]The carbon abundance entering the [C II] emission calculation is $\mathcal{A}_C \equiv$ C/H $= 2.69 \times 10^{-4}$ or $12 + \log$(C/H) $= 8.43$.

Downloaded from https://academic.oup.com/mnras/article/505/4/5543/6296656 by Scuola Normale Superiore Biblioteca user on 14 November 2022

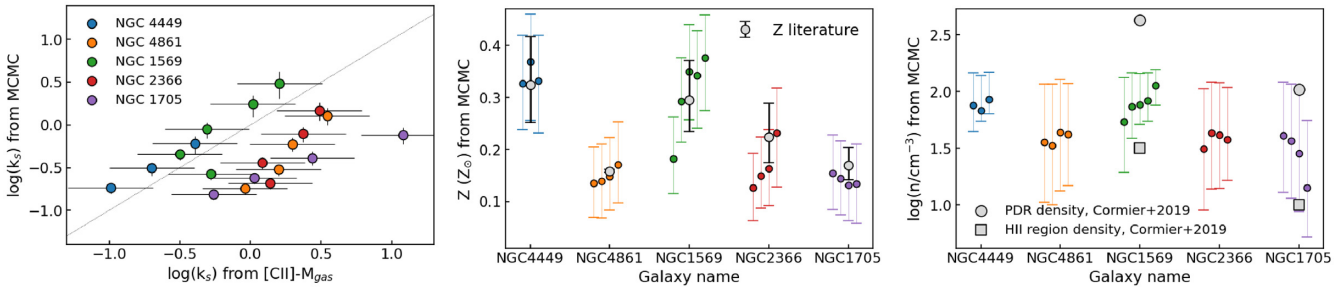

Figure 1. Left: Burstiness parameters derived with our model versus those derived from [C II] surface brightness by exploiting the Madden et al. (2020) relation. Each galaxy (colour-coded) has multiple κ_s estimates corresponding to different Σ_{SFR} bins. Centre: Scatter plot showing, for each galaxy, the best-fitting value of Z and 1σ errors returned by the MCMC in different Σ_{SFR} bins. Grey points with error bars represent the metallicity derived from the 12+log(O/H) values reported in the literature: NGC 4449 and NGC 4861 (Madden et al. 2013), NGC 1569 (McCormick et al. 2018), NGC 2366 (James et al. 2016), and NGC 1705 (Annibali et al. 2015). Right: Scatter plot showing, for each galaxy, the gas density from MCMC and the 1σ errors for the various Σ_{SFR} bins. For comparison, grey dots (grey squares) show the PDR (H II region) density derived by Cormier et al. (2019) in NGC 1569 and NGC 1705.

the Goodman Weare's Affine Invariant MCMC Ensemble sampler (Goodman & Weare 2010) adopting flat priors in the range of $0.0 \leq \log n \leq 4.0$, $-2 \leq \log Z \leq 0.0$, and $-1 \leq \log k_s \leq 2.5$, i.e. spanning all the physically reasonable parameter space.[2] We use the χ^2 likelihood function to determine the probability distribution function of the output parameters.

2.2 Model validation at low redshift

Before applying our model to galaxies in the EoR, we validate it on a sub-sample of five spatially resolved sources extracted from the Dwarf Galaxy Survey (DGS, Madden et al. 2013). Dwarf galaxies with their bursty star formation activity, low-metallicity, and low stellar mass are generally considered fair local analogues of high-z sources (e.g. Cormier et al. 2012; Ucci et al. 2019; Nanni et al. 2020). The five galaxies analysed here are NGC 4449, NGC 4861, NGC 1569, NGC 2366, and NGC 1705 for which we consider the spatially resolved HERSCHEL $\Sigma_{[C\,II]}$, $\Sigma_{[O\,III]}$, and *GALEX* FUV, and MIPS 24-μm measurements (converted to Σ_{SFR}) computed by De Looze et al. (2014) over pixels of physical size 114×114 pc^2.[3]For each galaxy, we aggregated the pixels in 0.5-dex bins in the range $\log(\Sigma_{SFR}/M_\odot\ yr^{-1}\ kpc^2) = [-3, 0.5]$ and associated to each of those bins the mean value of $\Sigma_{[C\,II]}$, $\Sigma_{[O\,III]}$.[4] These values are then fed as input to the model to compute the likelihood distribution of the (κ_s, Z, n) parameters over each bin.

In Fig. 1, for each galaxy we compare the (κ_s, Z, n) values with independent estimates in literature. The left-hand panel compares κ_s values obtained from our model with those estimated as $\kappa_s \propto \Sigma_{gas}^{1.4}/\Sigma_{SFR}$, i.e. by inverting the KS relation. This is done by inferring the Σ_{gas} in each Σ_{SFR} bin from the $\Sigma_{[C\,II]}$ using $L_{[C\,II]} - M_{gas}$ conversion factor in the DGS (Madden et al. 2020). Note that this assumption is rather uncertain as the $L_{[C\,II]} - M_{gas}$ relation involves integrated, rather than areal, quantities. We find that our κ_s estimates for NGC 4449 and NGC 1569 are in agreement within errors with those inferred by using the Madden et al. (2020) conversion factor. However, for NGC 1705, NGC 4861, and NGC 2366, 50 per cent of the bins show lower κ_s values with respect to those inferred from the $L_{[C\,II]} - M_{gas}$ conversion, falling at $\approx 1.5\,\sigma$ from the value estimated using the Madden et al. (2020) relation. This is likely because the errors on the κ_s derived applying the Madden et al. (2020) conversion consider only the uncertainty on the $L_{[C\,II]} - M_{gas}$ relation; thus, they are likely underestimated. In fact, we do not include other systematics inherent to the conversion from integrated to surface brightness values (e.g. contamination from the ionized gas phase partially contributing to the [C II] emission along the line of sight). In the central panel of Fig. 1, for each galaxy, we compare the metallicity obtained in each (Σ_{SFR}, $\Sigma_{[C\,II]}$, $\Sigma_{[O\,III]}$) bin, with global values reported in literature (Madden et al. 2013; Annibali et al. 2015; James et al. 2016; McCormick et al. 2018). We find excellent agreement as the different Z inferred in the various bins of each source are within the errors of the global galactic values. Finally, in the right-hand panel of Fig. 1, we compare the gas density inferred from our model over each (Σ_{SFR}, $\Sigma_{[C\,II]}$, $\Sigma_{[O\,III]}$) bin with literature values. This test can be performed only in two out of five sources (NGC 1569, NGC 1705) for which the average H II and PDR gas densities are available (Cormier et al. 2019). Cormier et al. (2019) derived the electron and PDR densities by simultaneously fitting mid-infrared lines from ionized gas ([Ar II], [Ar III], [S IV], [Ne II], [Ne III], [S III], [N II], [N III], [O III]) and FIR neutral gas tracers ([S III], [O I], [C II]) with CLOUDY models accounting for both phases and for the ionized-neutral boundary transition. Despite the caveat that systematic biases can be present when using different methods, we find a nice agreement between our values and those retrieved by Cormier et al. (2019). We note that the H II and PDR densities from Cormier et al. (2019) enclose the lower and upper bounds, respectively, of the density distribution derived with our method. This is expected as our n value represents the average density of the H II/PDR environment from which [O III] and [C II] line emission arises.

3 APPLYING THE MODEL IN THE EoR

More than 30 EoR galaxies have been so far detected and often spatially resolved in [C II] (e.g. Carniani et al. 2018a; Matthee et al. 2019, for compilations), and nine very bright galaxies (see Table 1) at $z \approx 6-9$ have been detected in [O III]. The list includes MACS1149-JD1 (Hashimoto et al. 2018), A2744-YD4 (Laporte et al. 2017b), MACS416-Y1 (Tamura et al. 2019), SXDF-NB1006-2 (Inoue et al. 2016), B14-65666 (Hashimoto et al. 2019), BDF3299 (Carniani et al. 2017), and J0121 J0235, J1211 (Harikane et al. 2020). All of them

[2]We publicly release the code, called GLAM (Galaxy Line Analyzer with MCMC), on GitHub (https://lvallini.github.io/MCMC_galaxyline_analyzer/) along with Jupyter notebooks that exemplify how to derive the (κ_s, Z, n) of any galaxy of interest for which $\Sigma_{[C\,II]}$, $\Sigma_{[O\,III]}$, and Σ_{SFR} are measured.
[3]Only pixels attaining surface brightness levels of signal to noise (S/N) >5 were taken into consideration by De Looze et al. (2014).
[4]The result of this procedure is detailed in Appendix A.

Downloaded from https://academic.oup.com/mnras/article/505/4/5543/6296656 by Scuola Normale Superiore Biblioteca user on 14 November 2022

Table 1. List of the EoR galaxies analysed in this work along with the input $\Sigma_{[\rm C\,II]}$, $\Sigma_{[\rm O\,III]}$, $\Sigma_{\rm SFR}$ values and the Z, κ_s n from the MCMC. We have assumed a fiducial 0.3-dex uncertainty for the $\Sigma_{\rm SFR}$. References as follows: M15 Maiolino et al. (2015), I16 Inoue et al. (2016), L17 Laporte et al. (2017b), C17 Carniani et al. (2017), H18 Hashimoto et al. (2018), H19 Hashimoto et al. (2019), T19 Tamura et al. (2019), B20 Bakx et al. (2020), HK20 Harikane et al. (2020), and C20 Carniani et al. (2020).

Name	z	$\log(\frac{\Sigma_{[\rm C\,II]}}{L_\odot\,\rm kpc^{-2}})$	$\log(\frac{\Sigma_{[\rm O\,III]}}{L_\odot\,\rm kpc^{-2}})$	$\log(\frac{\Sigma_{\rm SFR}}{\rm M_\odot\,yr^{-1}\,kpc^{-2}})$	$\log(Z/Z_\odot)$	$\log(\kappa_s)$	$\log(\frac{n}{\rm cm^{-3}})$	References
MACS1149-JD1	9.11	5.44 ± 0.25	6.55 ± 0.81	0.68	$-0.66^{+0.41}_{-0.59}$	$0.96^{+0.13}_{-0.34}$	$0.88^{+0.55}_{-0.19}$	H18, C20
A2744-YD4	8.38	5.62 ± 0.33	7.49 ± 0.24	1.40	$-0.64^{+0.39}_{-0.56}$	$1.89^{+0.26}_{-0.11}$	$1.28^{+0.50}_{-0.20}$	L17, C20
MACS0416-Y1	8.31	7.27 ± 1.21	8.57 ± 0.25	0.67	$-0.35^{+0.17}_{-0.17}$	$1.63^{+0.12}_{-0.12}$	$2.98^{+0.33}_{-0.27}$	T19, B20
SXDF-NB1006-2	7.21	6.31 ± 0.24	8.15 ± 0.22	0.84	$-0.65^{+0.40}_{-0.47}$	$1.65^{+0.10}_{-0.06}$	$2.21^{+0.64}_{-0.32}$	I16, C20
B14-65666	7.15	7.58 ± 0.33	8.18 ± 0.43	1.04	$-0.51^{+0.28}_{-0.28}$	$1.31^{+0.18}_{-0.18}$	$2.92^{+0.36}_{-0.19}$	H19
··· ClumpA	”	7.55 ± 0.38	7.97 ± 0.50	1.18	$-0.59^{+0.35}_{-0.36}$	$1.23^{+0.21}_{-0.23}$	$2.88^{+0.37}_{-0.20}$	H19
··· ClumpB	”	7.70 ± 0.64	7.94 ± 0.61	1.46	$-0.63^{+0.37}_{-0.37}$	$1.26^{+0.26}_{-0.24}$	$2.98^{+0.26}_{-0.25}$	H19
BDF3299	7.11	6.27 ± 0.13	7.41 ± 0.11	0.70	$-0.76^{+0.52}_{-0.54}$	$1.12^{+0.08}_{-0.05}$	$1.93^{+0.62}_{-0.41}$	M15, C17
J0217	6.20	7.19 ± 0.21	8.47 ± 0.27	1.28	$-0.48^{+0.29}_{-0.31}$	$1.82^{+0.12}_{-0.11}$	$2.67^{+0.50}_{-0.50}$	HK20
J0235	6.09	6.95 ± 0.45	8.40 ± 0.41	1.31	$-0.59^{+0.38}_{-0.35}$	$1.88^{+0.13}_{-0.14}$	$2.53^{+0.56}_{-0.31}$	HK20
J1211	6.02	7.17 ± 0.23	8.23 ± 0.35	1.25	$-0.57^{+0.34}_{-0.40}$	$1.56^{+0.17}_{-0.17}$	$2.56^{+0.60}_{-0.21}$	HK20

have been detected also in [C II], albeit at fainter fluxes with respect to [O III] (Maiolino et al. 2015; Hashimoto et al. 2019; Bakx et al. 2020; Carniani et al. 2020; Harikane et al. 2020), and therefore are suitable for use in our model.

From the line luminosity, and the sizes of the emitting regions ($r_{[\rm C\,II]}$, $r_{[\rm O\,III]}$) obtained by Carniani et al. (2020), we compute the surface brightness of each line as $\Sigma_{[\rm C\,II]} = L_{[\rm C\,II]}/2\pi r^2_{[\rm C\,II]}$, and $\Sigma_{[\rm O\,III]} = L_{[\rm O\,III]}/2\pi r^2_{[\rm O\,III]}$. $\Sigma_{\rm SFR}$ is inferred either from the UV-derived star formation rate ($\rm SFR_{UV}$) or, for sources detected in continuum by ALMA (A2744-YD4, MACS0416-Y1, B14-65666, J1211 and J0217), from the UV + IR luminosity ($\rm SFR = SFR_{UV} + SFR_{IR}$, Carniani et al. 2020) using the Kennicutt & Evans (2012) relations. In particular, Carniani et al. (2020) derived the infrared (IR) luminosity using a modified blackbody with dust temperature $T_{\rm d} = 40$ K and emissivity index $\beta = 1.5$ to reproduce the observed continuum measurements. The area of the star-forming region is taken equal to the UV emitting region, $\pi r^2_{\rm UV}$, following Carniani et al. (2018a) and Vallini et al. (2020). We stress two important caveats: (i) there is growing evidence that a large fraction of the high-z galaxy population is characterized by a multicomponent morphology (e.g. Maiolino et al. 2015; Jones et al. 2017; Matthee et al. 2017; Carniani et al. 2018a; Hashimoto et al. 2019), and (ii) this often leads to significant spatial offsets (up to several kpc) between [C II], [O III], dust continuum emission, and the star-forming regions traced by rest-frame UV light (Carniani et al. 2017; Bakx et al. 2020). Among the galaxies in our sample, B14-65666 and BDF3299 show a clear multicomponent morphology, MACS416-Y1 and BDF3299 have spatial offsets between [C II] and [O III]. B14-65666 has been spatially resolved in two clumps (A and B), which are both detected in [C II], [O III] and IR continuum (Hashimoto et al. 2019). This allow us to apply our model to B14-5666 and its two clumps separately. Doing the same for BDF3299 is impossible because the [C II] and the [O III] are not co-spatial. Hence, we warn the reader that for BDF3299 and MACS416-Y1, we use the global $\Sigma_{[\rm C\,II]}$,$\Sigma_{[\rm O\,III]}$, and $\Sigma_{\rm SFR}$ not considering the spatial displacement, an information that would require an additional parameter in our model.

The mean $\Sigma_{[\rm O\,III]}/\Sigma_{[\rm C\,II]}$ ratio of the EoR sample is $\approx$10 $\times$ higher than observed locally. As we will see in the next section, this has strong implications for the predicted (κ_s, Z, n) values. Hence, in the following, we pause to discuss whether such high values may be affected by observational biases due to beam smearing (Kohandel et al. 2019, 2020) or if instead they are produced by extreme conditions in the ISM of early galaxies.

3.1 Possible biases affecting high $\Sigma_{[\rm O\,III]}/\Sigma_{[\rm C\,II]}$ values

To study the $\Sigma_{[\rm O\,III]}/\Sigma_{[\rm C\,II]}$ expectation from a theoretical point of view, we consider a sample of 20 galaxies at $z = 7.7$ extracted from SERRA.[5] The sample extracted from SERRA is built by selecting central galaxies with stellar mass in the range $\log(M_*/M_\odot) = 8.0-10.1$, comparable to that spanned by the observed $z = 7-9$ sources in our EoR sample (Jones et al. 2020; Roberts-Borsani, Ellis & Laporte 2020).

In Fig. 2, we show the cutouts of *Iris*,[6] the most extended source in our sample. To perform a fair comparison with the [O III] and [C II] observations in low-z dwarf galaxies, we first derive $\Sigma_{[\rm C\,II]}$, $\Sigma_{[\rm O\,III]}$, $\Sigma_{\rm SFR}$ within circular patches of 100 pc diameter covering an area of 1.5 kpc $\times$ 1.5 kpc centred on each galaxy (see white circles in Fig. 2). Considering that typical UV size of sources at $z = 6-7$ is $\approx$0.5 $-$ 1.0 kpc (Shibuya et al. 2015, 2019) and that the [C II] half light radius is typically $r_{[\rm C\,II]} \approx 2.5 \pm 1.0$ (Carniani et al. 2018a; Matthee et al. 2019), the region covered by the patches is wide enough to include the ISM outskirts (see Fig. 2). We also compute the global $\Sigma_{[\rm C\,II]}$, $\Sigma_{[\rm O\,III]}$, $\Sigma_{\rm SFR}$ values in two different ways: (i) considering the (native) 30-pc resolution galaxy maps from SERRA, and dividing the [O III] ([C II]) luminosity of each galaxy at the half light radius, by the corresponding area, (ii) convolving the [O III] ([C II]) maps with

[5]SERRA follows the evolution of galaxies down to $z = 6$ with mass (spatial) resolution of the order of $10^4 M_\odot$ (30 pc at $z \approx 6$). The simulation adopts a multigroup radiative transfer version of the hydrodynamical code RAMSES (Teyssier 2002; Rosdahl et al. 2013) that includes thermochemical evolution via KROME (Grassi et al. 2014; Bovino et al. 2016; Pallottini et al. 2017), which is coupled to the radiation field (Pallottini et al. 2019; Decataldo et al. 2020), a state-of-the-art cosmological zoom-in simulation presented in Pallottini et al. (2017), Pallottini et al. (2019), and Pallottini et al. in preparation (). Stellar feedback includes SN explosions, OB/AGB winds, and both in thermal and turbulent forms (Pallottini et al. 2017). The [C II] and [O III] emission is obtained by post-processing the outputs with CLOUDY model grids (c17.0 version, Ferland et al. 2017) accounting for the internal structure of molecular clouds (Vallini et al. 2017; Pallottini et al. 2019).

[6]Galaxies extracted from SERRA (‘greenhouse’ in Italian) are named after flower species.

Downloaded from https://academic.oup.com/mnras/article/505/4/5543/6296656 by Scuola Normale Superiore Biblioteca user on 14 November 2022

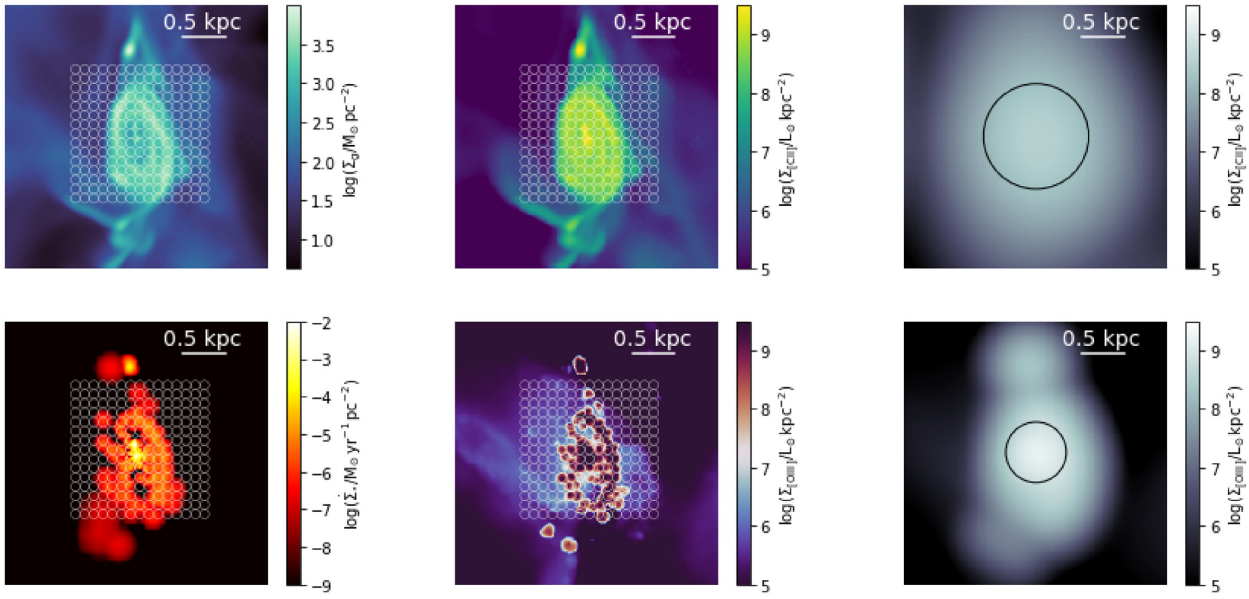

Figure 2. Cutouts of *Iris* (SERRA-04:46:4630), one the 20 galaxies extracted from the SERRA simulation (Pallottini et al. in preparation). We also overplot the circular patches of $d = 100$ pc covering a square of 1.5-kpc edge, used for our spatially resolved analysis (see text for details). Upper row: gas surface density (left), [C II] surface brightness (centre) at 30-pc resolution, and that obtained after convolving with $\theta = 0.2''$ beam (right). The half light radius is highlighted with a black circle. Bottom row: SFR surface density map (left), [O III] surface brightness at 30-pc resolution, and that obtained after convolving the simulation with a $\theta = 0.1''$ beam (right). The half light radius is indicated with a black circle.

a Gaussian kernel of 0.1-arcsec (0.2 arcsec) resolution and following the same procedure. The resolutions chosen are equal to the lower limits for the beam adopted in the observations analysed by Carniani et al. (2020). In both cases, Σ_{SFR} is the mean value computed at the half light radius of the [O III] emission.

The results of this analysis are shown in Fig. 3. There, we plot $\Sigma_{[C\,II]}$ versus $\Sigma_{[O\,III]}$ values for the 100 pc patches, and the galaxy-averaged values computed both at the 30-pc SERRA resolution and after convolution with the ALMA beam. The surface brightness of individual patches spans a wide range of down to $\Sigma_{[O\,III]} \simeq \Sigma_{[C\,II]} \approx 10^5 - 10^6\,L_\odot\,kpc^{-2}$, a value similar to that observed in local dwarfs. These faint regions are characterized by low $\Sigma_{SFR} \approx 10^{-2}\,M_\odot\,yr^{-1}\,kpc^{-2}$. However, these patch properties are not common in $z = 7$ galaxies; they deviate by $\gtrsim 2\sigma$ from the (luminosity weighted) mean, which is located at much higher $\Sigma_{[C\,II]} \approx 10^8\,L_\odot\,kpc^{-2}$, $\Sigma_{[O\,III]} \approx 10^{8.5}\,L_\odot\,kpc^{-2}$ surface brightness, or $\Sigma_{SFR} \approx 10^{1.5}\,M_\odot\,yr^{-1}\,kpc^{-2}$. This confirms that early sources are highly star-forming, with correspondingly bright [C II], [O III] arising from H II regions and dense PDR (Hollenbach & Tielens 1999; Vallini et al. 2015) associated with Giant Molecular Clouds, in agreement with finding from other groups (Katz et al. 2017; Arata et al. 2020).

Overall, 50 per cent (85 per cent) of the $\Sigma_{[O\,III]}$, $\Sigma_{[C\,II]}$, Σ_{SFR} galaxy-averaged values, at native resolution, fall within the 1σ (2σ) dispersion of the patches. In particular, their distribution peaks around the luminosity-weighted mean of the patches. The beam-convolved data shift towards slightly lower $\Sigma_{[C\,II]}$,$\Sigma_{[O\,III]}$ and Σ_{SFR}. However, the $\Sigma_{[O\,III]}/\Sigma_{[C\,II]}$ ratio remains constant as both the beam-convolved and the non-convolved values are $\approx 5-10\times$ higher than those measured in the local dwarfs on sub-kpc scales. The luminosity-weighted $\Sigma_{[O\,III]}/\Sigma_{[C\,II]}$ values on global galactic scales in the dwarf galaxies could potentially shift towards higher values, thus coming closer to those derived in the high-z sample. Nevertheless, from our simulation, we do not obtain any systematic shift of global values towards parameter regions that are not covered by *existing* patches; hence, we do not expect EoR observations to be affected by spurious bias effects.

We conclude that high-z galaxies observed so far seem to show rather extreme ISM properties, namely high-Σ_{SFR}, high-$\Sigma_{[O\,III]}/\Sigma_{[C\,II]}$ values. This is expected as they have been selected to be the brightest sources at those redshifts. Finally, if we compare the beam-averaged values of SERRA with the observed ones, we find a very good agreement with the majority of the sources, even though MACS1149-JD1 ($z = 9.1$) and AZ744-YD4 ($z = 8.38$) have lower $\Sigma_{[C\,II]}$ values than the global values inferred from SERRA at $z = 7.7$, and also higher Σ_{SFR} when compared with the patches falling in the same range of $\Sigma_{[O\,III]}$, $\Sigma_{[C\,II]}$.

4 RESULTS

The $\Sigma_{[C\,II]}$, $\Sigma_{[O\,III]}$ and Σ_{SFR} (along with their uncertainties) in the EoR sample allow us to run our model and derive the posterior probability distributions of the free parameters. The results, along with their 1σ errors, are gathered in Table 1, while in Appendix B, we report all the corner plots showing the 2D posterior probability distributions of (κ_s, Z, n) for each of the galaxy/sub-component analysed in this work. [7] As a first step, we focus on to the determination of the burstiness parameter κ_s. All the joint [O III]–[C II] emitters in the EoR sample have $1.0 < \log\kappa_s < 2.0$, meaning that all of them are starburst galaxies with upward deviations from the KS relation. These values are also higher than $\log\kappa_s = 0.3$ found by V20 for COS3018, a Lyman Break Galaxy (LBG) at $z = 6.6$, with the same method applied to [C II] and C III] emission data. While, in principle, using C III] or [O III] should return consistent (κ_s, Z, n) values if applied

[7]The current work focuses on a simple situation where the slab geometry, a linear gas-to-dust ratio as a function of metallicity, and a uniform C/O abundance ratio are assumed. The derived parameters can thus have intrinsically larger uncertainties.

Downloaded from https://academic.oup.com/mnras/article/505/4/5543/6296656 by Scuola Normale Superiore Biblioteca user on 14 November 2022

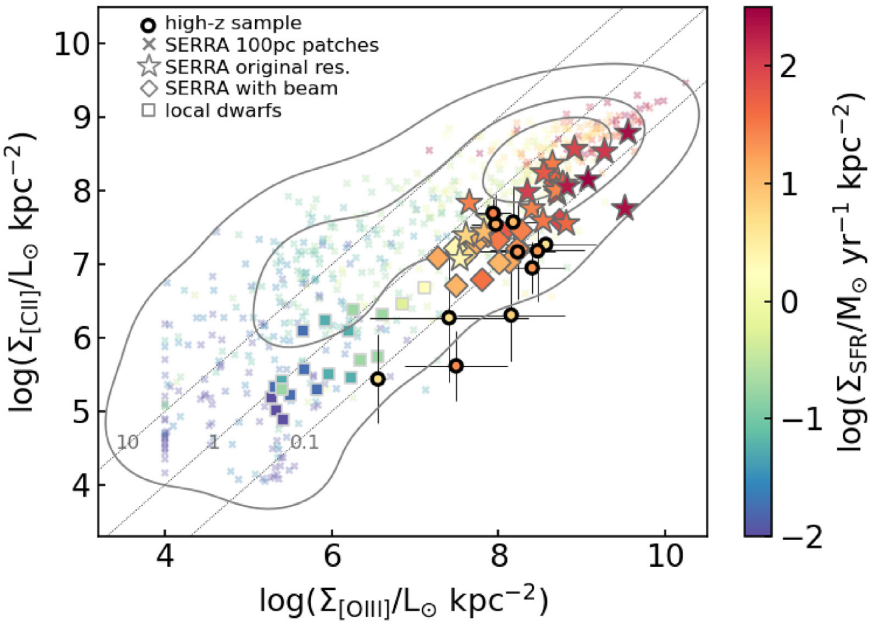

Figure 3. $\Sigma_{[\mathrm{O\,III}]}$ versus $\Sigma_{[\mathrm{C\,II}]}$ relation for the high-z galaxies analysed in this work (circles with error bars) colour-coded as a function of Σ_{SFR}. The stars represent the result for the 20 sources extracted from SERRA at $z = 7$ at 30-pc resolution. The results obtained when convolving the simulation with the ALMA beam are instead plotted with diamonds. Small crosses represent values extracted from 100-pc scale ISM patches within SERRA galaxies. The 1σ, 2σ, and 3σ levels of the patches distribution are plotted in grey. The $z = 0$ dwarf galaxy sample is denoted by squares. To guide the eye, we indicate the 1:1 relation (and the $\pm$1dex dispersion around it) with dotted black lines.

on a galaxy detected in all the three lines, modulo variations with Z of the C/O abundance ratio, dust extinction effects on the C III] luminosity could decrease κ_{s} if the C III] value is underestimated.

The κ_{s} derived with our method can be used to constrain the (resolved) gas depletion time $t_{\mathrm{dep}} \approx \Sigma_{\mathrm{gas}}/\Sigma_{\mathrm{SFR}} \propto \kappa_s^{-(1/1.4)} \Sigma_{\mathrm{SFR}}^{(1/1.4)-1}$ of the galaxies. High κ_{s} values result in short depletion times, $t_{\mathrm{dep}} = 6-49$ Myr. This is in line with resolved t_{dep} values derived in a handful of dusty star-forming galaxies (DSFGs) at $z \approx 3.5-5$: $t_{\mathrm{dep}} = 50-200$ Myr (Hodge et al. 2015), $t_{\mathrm{dep}} = 1-30$ Myr (Rybak et al. 2020), and $t_{\mathrm{dep}} = 12-357$ Myr (Rizzo et al. 2021). Our analysis thus suggests that joint [C II]–[O III] emitters, despite not being as dusty as DSFGs, share comparable levels of star formation activity. They also seem to be characterized by ISM conditions favouring an efficient conversion of gas into stars, carving H II regions that shine conspicuously in [O III] emission.

4.1 Relative role of (κ_{s}, Z, n) on $\Sigma_{[\mathrm{O\,III}]}/\Sigma_{[\mathrm{C\,II}]}$

To broadly quantify possible trends between (κ_{s}, Z, n) and the $\Sigma_{[\mathrm{O\,III}]}/\Sigma_{[\mathrm{C\,II}]}$, in Fig. 4 we present the best-fitting linear regression between $\log(\Sigma_{[\mathrm{O\,III}]}/\Sigma_{[\mathrm{C\,II}]})$ and $\log \kappa_{\mathrm{s}}$, $\log n$, $\log Z$, separately. For the burstiness parameter, we find the following relation:

$$\log(\Sigma_{[\mathrm{O\,III}]}/\Sigma_{[\mathrm{C\,II}]}) = \alpha \log \kappa_{\mathrm{s}} + \beta \tag{6}$$

with $\alpha = 1.04 \pm 0.41$, and $\beta = -0.42 \pm 0.62$. The correlation is thus linear and can be explained by considering that higher starbursting conditions produce more extended ionized layers (Ferrara et al. 2019) in which [O III]88 μm is excited. Equation (6) can be readily used to estimate the global deviation from the KS relation of EoR galaxies once resolved ALMA [O III] and [C II] observations are obtained.

For what concerns the gas density we obtain:

$$\log(\Sigma_{[\mathrm{O\,III}]}/\Sigma_{[\mathrm{C\,II}]}) = \alpha \log n + \beta \tag{7}$$

with $\alpha = -0.38 \pm 0.21$ and $\beta = 2.00 \pm 0.52$. The negative slope can be explained in terms of the different critical density of [O III]88 μm ($n_{\mathrm{c,O\,III}} = 500\,\mathrm{cm}^{-3}$ for collisions with free electrons) and [C II] ($n_{\mathrm{c,C\,II}} = 3300\,\mathrm{cm}^{-3}$, for collisions with neutrals). For galaxies with $n_{\mathrm{c,O\,III}} < n < n_{c,\mathrm{C\,II}}$, the [O III]/[C II] luminosity ratio drops, and so does the surface brightness one (see Fig. 4, right-hand panel). If the average density of a galaxy is below $n_{\mathrm{c,O\,III}}$, and thus also below the $n_{\mathrm{c,C\,II}}$, the gas density does not affect the [O III]/[C II] ratio anymore leaving the burstiness of the source as the most important physical mechanism boosting the [O III]/[C II] ratio. Finally, despite the increasing [O III]/[C II] trend towards lower Z observed in dwarf galaxies (Cormier et al. 2015), we do not find any significant correlation between $\log(\Sigma_{[\mathrm{O\,III}]}/\Sigma_{[\mathrm{C\,II}]})$ and gas metallicity.

To quantitatively assess the importance of the parameters, we also performed a principal component analysis (PCA). PCA is a linear transformation technique by which a set of variables (in our case κ_{s}, n, Z, $\Sigma_{[\mathrm{O\,III}]}/\Sigma_{[\mathrm{C\,II}]}$) are combined into orthogonal *principal components* (PC). Successive components account for decreasing variance in the sample, under the constraint that each PC is orthogonal to the previous ones. In order to perform the PCA, we first normalize the variables to zero mean in logarithmic space:

$$x_1 = \log(\kappa_{\mathrm{s}}) - \langle \log(\kappa_{\mathrm{s}}) \rangle \tag{8}$$

$$x_2 = \log(n) - \langle \log(n) \rangle \tag{9}$$

$$x_3 = \log(Z) - \langle \log(Z) \rangle \tag{10}$$

$$x_4 = \log(\Sigma_{[\mathrm{O\,III}]}/\Sigma_{[\mathrm{C\,II}]}) - \langle \log(\Sigma_{[\mathrm{O\,III}]}/\Sigma_{[\mathrm{C\,II}]}) \rangle \tag{11}$$

and then we derive enough PCs to explain 99 per cent of the sample variance. In our case, we need three components (PC1, PC2, and PC3) that account for 69 per cent, 28 per cent, and 2 per cent of the variance, respectively:

Downloaded from https://academic.oup.com/mnras/article/505/4/5543/6296656 by Scuola Normale Superiore Biblioteca user on 14 November 2022

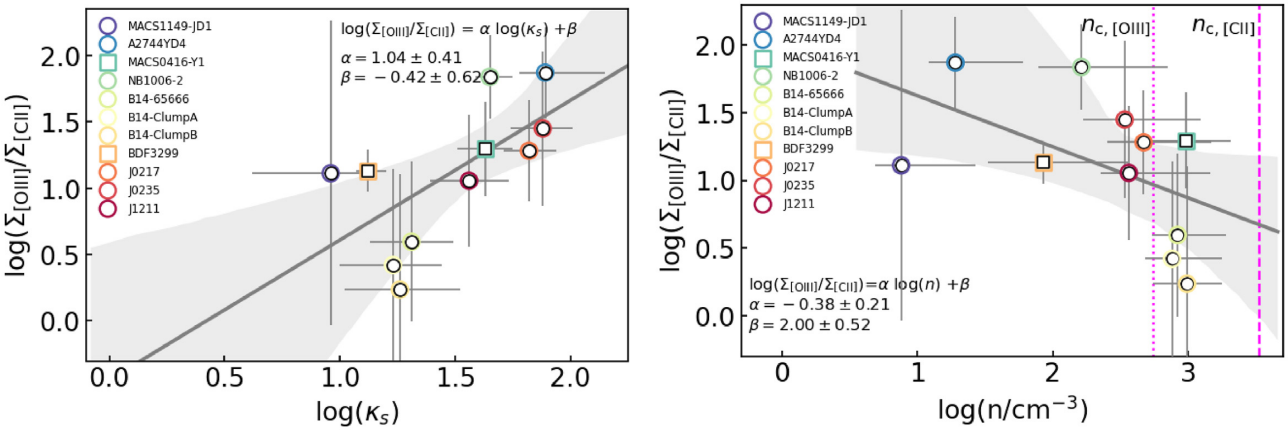

Figure 4. Left-hand panel: Best-fitting $\log(\Sigma_{[O\,III]}/\Sigma_{[C\,II]})$-$\log\kappa_s$ relation and its 1σ dispersion (black line and shaded area) for the high-z joint [C II]–[O III] sample analysed in this work. Right-hand panel: Best-fitting $\log(\Sigma_{[O\,III]}/\Sigma_{[C\,II]})$–$\log n$ relation and its 1σ dispersion. The magenta vertical lines represent the critical densities of [O III] (dotted) and [C II] (dashed) transitions. In both panels, the two sources with spatial displacement between [C II], [O III], and UV – for which our model assumption of a single gas slab could introduce a bias in the derivation of the trends – are indicated with a different symbol (square).

$$\mathrm{PC1} = 0.04x_1 - 0.86x_2 - 0.06x_3 + 0.50x_4 \quad (12)$$

$$\mathrm{PC2} = -0.60x_1 - 0.41x_2 - 0.10x_3 - 0.68x_4 \quad (13)$$

$$\mathrm{PC3} = -0.80x_1 + 0.27x_2 - 0.04x_3 - 0.54x_4. \quad (14)$$

The first eigenvector, PC1, is dominated by the gas density while PC2 and PC3 are dominated by κ_s. The metallicity is the least influential parameter in all the PCs. Given that PC3 accounts for only ∼2 per cent of the variance, it can be exploited for establishing an optimized view of the parameter space defined by $\log\kappa_s$, $\log n$, $\log Z$, and $\log(\Sigma_{[O\,III]}/\Sigma_{[C\,II]})$ thus giving:

$$\log\left(\frac{\Sigma_{[O\,III]}}{\Sigma_{[C\,II]}}\right) = 0.16 + 1.5\log\kappa_s - 0.5\log n + 0.07\log Z. \quad (15)$$

This relation is especially useful from a theoretical standpoint, as it combines in a single expression the dependence of the [O III]/[C II] ratio on the three main physical parameters of the problem. As a caveat, we note that, although in general PCA is very effective in isolating correlations among parameters, both the sample size and the metallicity range spanned here are small. Hence, further analysis on larger samples would be beneficial. Alternatively, equations (6) and (7) can be adopted to infer κ_s or n from measured $\Sigma_{[O\,III]}/\Sigma_{[C\,II]}$ values in galaxies lacking information on all parameters.

To summarize, our analysis suggests that high $\Sigma_{[O\,III]}/\Sigma_{[C\,II]}$ values so far measured in high-z galaxies are likely produced by ongoing starbursts. Note that also several spectral energy distribution (SED) fitting analyses (e.g. Laporte et al. 2017b; Jones et al. 2020; Roberts-Borsani et al. 2020) and cosmological simulations (Pallottini et al. 2017, 2019; Arata et al. 2020) point towards EoR sources being characterized by intermittent star formation histories with separated bursts of star formation. This highlights the importance of using multiparameter MCMC approaches to derive the metallicity from [O III]/[C II] ratios (see Fig. 5) and represents an attempt in the direction suggested by Harikane et al. (2020), who pointed out that the metallicity dependence of the [O III]/[C II] ratio cannot be easily disentangled from variations[8] in the ionization parameter and n.

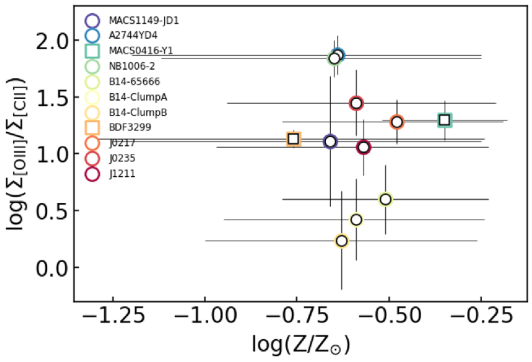

Figure 5. The $\log(\Sigma_{[O\,III]}/\Sigma_{[C\,II]})$–$\log Z$ scatter plot for the high-z sources analysed in this work. The two sources with spatial displacement between [C II], [O III], and UV are indicated with a different symbol (square).

4.2 Metallicity and density in the EoR sample

In this section, we discuss the major implications of the overall conditions of the ISM in EoR galaxies as inferred from the $\Sigma_{[O\,III]}/\Sigma_{[C\,II]}$ ratios and we compare them with findings of other works in the literature. Despite the high-redshift range spanned by the sample ($z \approx 6$–9), we find relatively high metallicities, $Z \approx 0.2 - 0.5\,Z_\odot$, and a wide range of densities, $\log(n/\mathrm{cm}^{-3}) \approx 0.7$–$3.0$. This seems to indicate that joint [O III]–[C II] emitters so far detected in the EoR have a fairly enriched ISM with some of the sources (MACS0416-Y1, B14-65666) presenting also high $\log n > 2.5$ average densities. These values are in line with results obtained from zoom-in cosmological simulations of galaxies with comparable stellar mass (Pallottini et al. 2017, 2019).

In Fig. 6, we compare our findings with results from two recently published independent analysis (Jones et al. 2020; Yang & Lidz 2020). Jones et al. (2020) – with the aim of studying the mass−metallicity relation (MZR, Maiolino & Mannucci 2019, and references therein) – derived the (O/H) abundance in all but three sources of our sample. The oxygen abundance was inferred from the [O III]88 μm/Hβ ratio, where the Hβ has been computed

[8]We caution the reader that in this work, we have assumed a fixed O/C abundance. Recent simulations from Arata et al. (2020) suggest that the increasing trend can be ascribed to enhanced O/C ratios at low-Z (e.g. Steidel et al. 2016; Berg et al. 2019).

Downloaded from https://academic.oup.com/mnras/article/505/4/5543/6296656 by Scuola Normale Superiore Biblioteca user on 14 November 2022

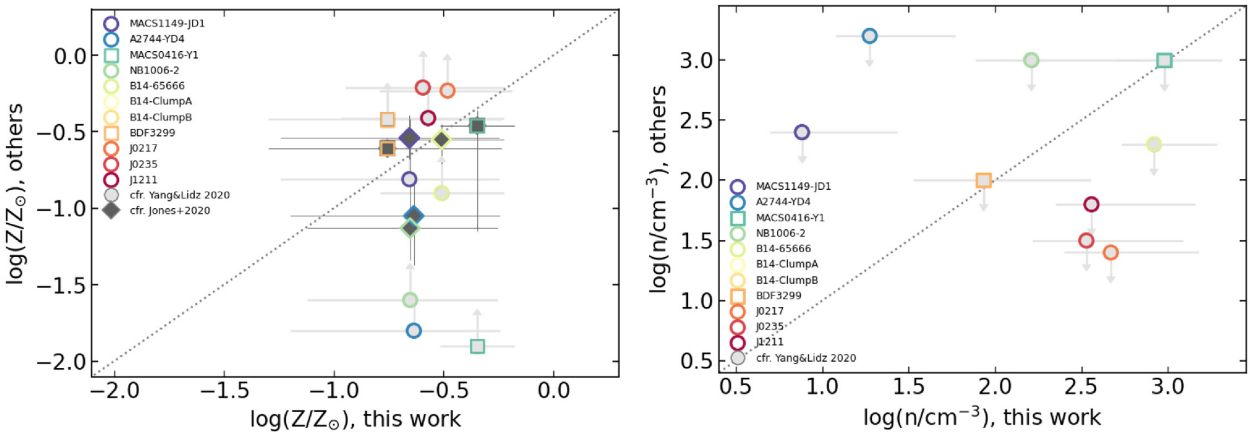

Figure 6. Comparison between metallicity (left-hand panel) and gas density (right-hand panel) derived in this work and those obtained by Jones et al. (2020) (black diamonds) and Yang & Lidz (2020) (grey circles). The dotted line in the two panels represents the 1:1 relation. The two sources with spatial displacement between [C II], [O III], and UV are indicated with a different symbol (square).

from the photometrically derived SFR of each galaxy. Yang & Lidz (2020), instead, presented a physically motivated analytical model for the [O III]88 μm and [O III]52 μm line emission, relating the [O III]88 μm/SFR ratio of a galaxy to the average electron density and metallicity in the H II regions. Due to the $n_e - Z$ degeneracy of [O III]88 μm emissivity equations from Yang & Lidz (2020), they compute the resulting 2D posteriors in the $n - Z$ plane. They quote the 1σ lower bound on Z, and the 1σ upper bound on $\log n$ as the most robust results from their analysis, which we therefore consider in our comparison.

The metallicities[9] derived with the MCMC are in nice agreement with those inferred from Jones et al. (2020), which, in line with our previous discussion, pointed out the relatively high values of metallicities and the lack of strong evolution of the MZR towards $z = 7-8$. Our Z values also agree within the errors with the lower limits on metallicity from Yang & Lidz (2020). On the other hand, we exceed their upper bounds on the H II region electron density (n_e) in four out of nine sources.

This is expected, as with our model we constrain the mean gas density of two connected environments, namely the H II regions (dominating the [O III] emission) and the PDRs (dominating the [C II] emission). The PDRs are generally characterized by higher densities ($\log n = 2-4$) with respect to that of H II regions ($\log n_e = 0-3$), as also outlined in the model validation section when comparing n_{PDR} and $n_{H\,II}$ derived by Cormier et al. (2019) in local dwarf galaxies with those inferred with our model. Finally, note that the values of n are in line with the mean gas density in the central regions of the SERRA galaxies characterized by $\log n = 2.5 - 3.0$ (Pallottini et al. 2019).

5 CONCLUSIONS

In this work, we have studied the origin of the high $\Sigma_{[O\,III]}/\Sigma_{[C\,II]}$ ratios observed in ALMA-detected EoR galaxies. We have used a model that relates the $\Sigma_{[O\,III]}/\Sigma_{[C\,II]}$ and Σ_{SFR} of the galaxy to three quantities: the deviation from the KS relation, the gas metallicity, and the gas density of early galaxies. We have tested our method on a sample of low-z dwarf sources with measured $\Sigma_{[C\,II]}$, $\Sigma_{[O\,III]}$, Σ_{SFR}, finding an overall good agreement between our results and previous data in the literature. The method has then been applied to the (only) nine galaxies at $z > 6$ jointly detected in [C II] and [O III]. Our main findings are as follows:

(i) High ($\Sigma_{[O\,III]}/\Sigma_{[C\,II]} \approx 30$) ratios are not due to observational biases, but they genuinely arise from the extreme gas conditions prevailing in these early galaxies.

(ii) According to our model, the observed $\Sigma_{[O\,III]}/\Sigma_{[C\,II]}$ ratios correspond to $\kappa_s = 10-100$, i.e. upward Σ_{SFR} deviations by 10–100$\times$ from the Kennicutt−Schmidt relation.

(iii) We use κ_s to constrain the (resolved) gas depletion time $t_{dep} = 6 - 49$ Myr. Such low values are in line with resolved t_{dep} measurements of dusty star-forming galaxies at $z \approx 3-5$.

(iv) A principal component analysis suggests that $\Sigma_{[O\,III]}/\Sigma_{[C\,II]}$ mostly depend on κ_s with a secondary anticorrelation with gas density.

(v) The high κ_s (low t_{dep}) suggests that [C II]–[O III] emitters are characterized by ISM conditions favouring an efficient conversion of gas into stars, with starburst episodes producing bright [O III] emission from H II regions and hotter dust temperature as recently found by Sommovigo et al. (2021).

(vi) Linear regressions between $\Sigma_{[O\,III]}/\Sigma_{[C\,II]}$ and one parameter at the time return the following relations: $\Sigma_{[O\,III]}/\Sigma_{[C\,II]} \propto \kappa_s$, and $\Sigma_{[O\,III]}/\Sigma_{[C\,II]} \propto n^{-0.4}$. However, we do not find evidence for a relation with gas metallicity.

(vii) Gas metallicity and density are relatively high ($Z = 0.1-0.5Z_\odot$, and $n = 10^{1-3}$cm^{-3}) in the nine sample galaxies, also in agreement with findings from Jones et al. (2020) and Yang & Lidz (2020).

Our method will allow to constrain the star formation law at sub-kpc scales in early galaxies via $\Sigma_{[O\,III]}/\Sigma_{[C\,II]}$ ratios by boosting ALMA spatial resolution with the help of gravitational lensing.

ACKNOWLEDGEMENTS

LV, AF, SC, and AP acknowledge support from the ERC Advanced Grant INTERSTELLAR H2020/740120 (PI: Ferrara). Any dissemination of results must indicate that it reflects only the author's view and that the Commission is not responsible for any use that may be made of the information it contains. Partial support from the Carl Friedrich von Siemens-Forschungspreis der Alexander von Humboldt-Stiftung Research Award is kindly acknowledged (AF).

[9]We convert 12+(O/H) to Z assuming $12 + (O/H)_\odot = 8.69$ (Asplund et al. 2009).

Downloaded from https://academic.oup.com/mnras/article/505/4/5543/6296656 by Scuola Normale Superiore Biblioteca user on 14 November 2022

We acknowledge the CINECA award under the ISCRA initiative for the availability of high-performance computing resources and support from the Class B project SERRA HP10BPUZ8F. We acknowledge use of Astropy (Astropy Collaboration 2018), MATPLOTLIB (Hunter 2007), NUMPY (Harris et al. 2020), Seaborn (Waskom 2021), SCIPY (Virtanen et al. 2020), and Pandas (McKinney 2010). LV thanks Laura Sommovigo for fruitful discussions. We thank the reviewer for useful suggestions that improved the quality of the paper.

DATA AVAILABILITY

We release the code, called GLAM (Galaxy Line Analyzer with MCMC) for the derivation of the (κ_s, Z, n) from $\Sigma_{[O\,III]}/\Sigma_{[C\,II]}$ observations on Github at: https://lvallini.github.io/MCMC_galaxyline_analyzer/. The SERRA data used in this article were accessed from the computational resources available to the Cosmology Group at Scuola Normale Superiore, Italy.

REFERENCES

Annibali F., Tosi M., Pasquali A., Aloisi A., Mignoli M., Romano D., 2015, AJ, 150, 143
Arata S., Yajima H., Nagamine K., Abe M., Khochfar S., 2020, MNRAS, 498, 5541
Asplund M., Grevesse N., Sauval A. J., Scott P., 2009, ARA&A, 47, 481
Astropy Collaboration, 2018, AJ, 156, 123
Bakx T. J. L. C. et al., 2020, MNRAS, 493, 4294
Berg D. A., Erb D. K., Henry R. B. C., Skillman E. D., McQuinn K. B. W., 2019, ApJ, 874, 93
Béthermin M. et al., 2020, A&A, 643, A2
Bovino S., Grassi T., Capelo P. R., Schleicher D. R. G., Banerjee R., 2016, A&A, 590, A15
Bradač M. et al., 2017, ApJ, 836, L2
Calura F. et al., 2021, MNRAS, 500, 3083
Capak P. L. et al., 2015, Nature, 522, 455
Carilli C. L., Walter F., 2013, ARA&A, 51, 105
Carniani S. et al., 2017, A&A, 605, A42
Carniani S. et al., 2018a, MNRAS, 1042
Carniani S. et al., 2020, MNRAS, 499, 5136
Carniani S., Maiolino R., Smit R., Amorín R., 2018b, ApJ, 854, L7
Cormier D. et al., 2012, A&A, 548, A20
Cormier D. et al., 2015, A&A, 578, A53
Cormier D. et al., 2019, A&A, 626, A23
De Looze I. et al., 2014, A&A, 568, A62
Decataldo D., Ferrara A., Pallottini A., Gallerani S., Vallini L., 2017, MNRAS, 471, 4476
Decataldo D., Lupi A., Ferrara A., Pallottini A., Fumagalli M., 2020, MNRAS, 497, 4718
Díaz-Santos T. et al., 2017, ApJ, 846, 32
Ferland G. J. et al., 2017, RMxAA, 53, 385
Ferrara A., Vallini L., PallottiniA., Gallerani, S., Carniani S., Kohandel M., Decataldo D., Behrens C., 2019, MNRAS, 489, 1
Foreman-Mackey D. et al., 2013, Astrophysics Source Code Library, record ascl:1303.002.
Fujimoto S. et al., 2019, ApJ, 887, 107
Fujimoto S. et al., 2020, ApJ, 900, 1
Ginolfi M. et al., 2020, A&A, 633, A90
Goodman J., Weare J., 2010, CAMCOS, 5, 65
Grassi T., Bovino S., Schleicher D. R. G., Prieto J., Seifried D., Simoncini E., Gianturco F. A., 2014, MNRAS, 439, 2386
Harikane Y. et al., 2020, ApJ, 896, 93
Harris C. R. et al., 2020, Nature, 585, 357
Hashimoto T. et al., 2018, Nature, 557, 392
Hashimoto T. et al., 2019, PASJ, 71, 71
Herrera-Camus R. et al., 2015, ApJ, 800, 1
Herrera-Camus R. et al., 2021, A&A, 649, A31
Hodge J. A., Riechers D., Decarli R., Walter F., Carilli C. L., Daddi E., Dannerbauer H., 2015, ApJ, 798, L18
Hollenbach D. J., Tielens A. G. G. M., 1999, RMP, 71, 173
Hunter J. D., 2007, Comput. Sci. Eng., 9, 90
Inoue A. K. et al., 2016, Science, 352, 1559
James B. L., Auger M., Aloisi A., Calzetti D., Kewley L., 2016, ApJ, 816, 40
Jones G. C., Willott C. J., Carilli C. L., Ferrara A., Wang R., Wagg J., 2017, ApJ, 845, 175
Jones T., Sanders R., Roberts-Borsani G., Ellis R. S., Laporte N., Treu T., Harikane Y., 2020, ApJ, 903, 150
Katz H., Kimm T., Sijacki D., Haehnelt M. G., 2017, MNRAS, 468, 4831
Kennicutt Robert C. J., 1998, ApJ, 498, 541
Kennicutt R. C., Evans N. J., 2012, ARA&A, 50, 531
Knudsen K. K., Richard J., Kneib J.-P., Jauzac M., Clément B., Drouart G., Egami E., Lindroos L., 2016, MNRAS, 462, L6
Kohandel M., Pallottini A., Ferrara A., Zanella A., Behrens C., Carniani S., Gallerani S., Vallini L., 2019, MNRAS, 487, 3007
Kohandel M., Pallottini A., Ferrara A., Carniani S., Gallerani S., Vallini L., Zanella A., Behrens C., 2020, MNRAS, 499, 1250
Lagache G., Cousin M., Chatzikos M., 2018, A&A, 609, A130
Laporte N. et al., 2017a, ApJ, 837, L21
Laporte N., Nakajima K., Ellis R. S., Zitrin A., Stark D. P., Mainali R., Roberts-Borsani G. W., 2017b, ApJ, 851, 40
Le Fèvre O. et al., 2020, A&A, 643, A1
Lupi A., Pallottini A., Ferrara A., Bovino S., Carniani S., Vallini L., 2020, MNRAS 496, 5160
Luridiana V., Morisset C., Shaw R. A., 2015, MNRAS, 573, A42
Madden S. C. et al., 2013, PASP, 125, 600
Madden S. C. et al., 2020, A&A, 643, A141
Maiolino R. et al., 2015, MNRAS, 452, 54
Maiolino R., Mannucci F., 2019, A&A Rev., 27, 3
Matthee J. et al., 2017, ApJ, 851, 145
Matthee J. et al., 2019, ApJ, 881, 124
McCormick A. et al., 2018, MNRAS, 477, 699
McKinney W., 2010, in Proceedings of the 9th Python in Science Conference. p. 56
McKinney J., Armus L., Pope A., Díaz-Santos T., Charmandaris V., Inami H., Song Y., Evans A. S., 2021, ApJ, 908, 238
Moriwaki K. et al., 2018, MNRAS, 481, L84
Nanni A., Burgarella D., Theulé P., Côté B., Hirashita H., 2020, A&A, 641, A168
Olsen K., Greve T. R., Narayanan D., Thompson R., Davé R., Niebla Rios L., Stawinski S., 2017, ApJ, 846, 105
Palay E., Nahar S. N., Pradhan A. K., Eissner W., 2012, MNRAS, 423, L35
Pallottini A. et al., 2019, MNRAS, 487, 1689
Pallottini A., Ferrara A., Bovino S., Vallini L., Gallerani S., Maiolino R., Salvadori S., 2017, MNRAS, 471, 4128
Pentericci L. et al., 2016, ApJ, 829, L11
Pettini M., Pagel B. E. J., 2004, MNRAS, 348, L59
Rizzo F., Vegetti S., Fraternali F., Stacey H., Powell D., 2021, preprint (arXiv:2102.05671)
Roberts-Borsani G. W., Ellis R. S., Laporte N., 2020, MNRAS, 497, 3440
Rosdahl J., Blaizot J., Aubert D., Stranex T., Teyssier R., 2013, MNRAS, 436, 2188
Rybak M., Hodge J. A., Vegetti S., van der Werf P., Andreani P., Graziani L., McKean J. P., 2020, MNRAS, 494, 5542
Shibuya T., Ouchi M., Harikane Y., 2015, ApJS, 219, 15
Shibuya T., Ouchi M., Harikane Y., Nakajima K., 2019, ApJ, 871, 164
Smit R. et al., 2018, Nature, 553, 178
Sommovigo L., Ferrara A., Carniani S., Zanella A., Pallottini A., Gallerani S., Vallini L., 2021, MNRAS, 503, 4878
Stacey G. J., Geis N., Genzel R., Lugten J. B., Poglitsch A., Sternberg A., Townes C. H., 1991, ApJ, 373, 423
Stark D. P. et al., 2015, MNRAS, 450, 1846
Steidel C. C., Strom A. L., Pettini M., Rudie G. C., Reddy N. A., Trainor R. F., 2016, ApJ, 826, 159
Tamura Y. et al., 2019, ApJ, 874, 27
Teyssier R., 2002, A&A, 385, 337

Downloaded from https://academic.oup.com/mnras/article/505/4/5543/6296656 by Scuola Normale Superiore Biblioteca user on 14 November 2022

Ucci G. et al., 2019, MNRAS, 483, 1295
Vallini L., Gallerani S., Ferrara A., Baek S., 2013, MNRAS, 433, 1567
Vallini L., Gallerani S., Ferrara A., Pallottini A., Yue B., 2015, ApJ, 813, 36
Vallini L., Ferrara A., Pallottini A., Gallerani S., 2017, MNRAS 467, 1300
Vallini L., Ferrara A., Pallottini A., Carniani S., Gallerani S., 2020, MNRAS, 495, L22
Virtanen P. et al., 2020, Nature Methods, 17, 261
Waskom M. L., 2021, J. Open Source Softw., 6, 3021
Willott C. J., Carilli C. L., Wagg J., Wang R., 2015, ApJ, 807, 180
Wolfire M. G., McKee C. F., Hollenbach D., Tielens A. G. G. M., 2003, ApJ, 587, 278
Yang S., Lidz A., 2020, MNRAS, 499, 3417

APPENDIX A: LOW-z DWARF GALAXY SAMPLE: DATA AND PARAMETERS

Fig. A1 shows the $\Sigma_{\rm SFR}$–$\Sigma_{\rm [C\,II]}$ relation for the five dwarf galaxies considered in this work (grey points). For the five galaxies, we highlight the $\Sigma_{\rm SFR}$ bins over which we compute the average $\Sigma_{\rm [O\,III]}$ and $\Sigma_{\rm [C\,II]}$ (coloured big points with error bars) used in our method validation at low-z. Furthermore, in Table A1, we list the metallicity values of dwarf galaxies from literature against which we test our validation. As a caveat note that different methods were used for deriving the metallicities referenced in Table A1. More precisely, James et al. (2016) derived the gas-phase metallicity with narrow-band images based on the R23 method, which is offset from the direct-temperature method by 0.23 dex. Annibali et al. (2015) used the multiobject slit spectroscopy and obtained the gas-phase metallicity with the direct-temperature method. Madden et al. (2013) derived the metallicity using the R23 method, while McCormick et al. (2018) have obtained metallicity using the Pettini & Pagel (2004) method based on the ([O III]/H β)/([NII]/H α) ratio.

Table A1. Oxygen abundance of the five dwarf galaxies considered in this work.

Galaxy	12+(O/H)	Reference
NGC 4449	8.20 ± 0.11	Madden et al. (2013)
NGC 4861	7.89 ± 0.01	Madden et al. (2013)
NGC 1569	8.16 ± 0.10	McCormick et al. (2018)
NGC 2366	8.04 ± 0.11	James et al. (2016)
NGC 1705	7.91 ± 0.08	Annibali et al. (2015)

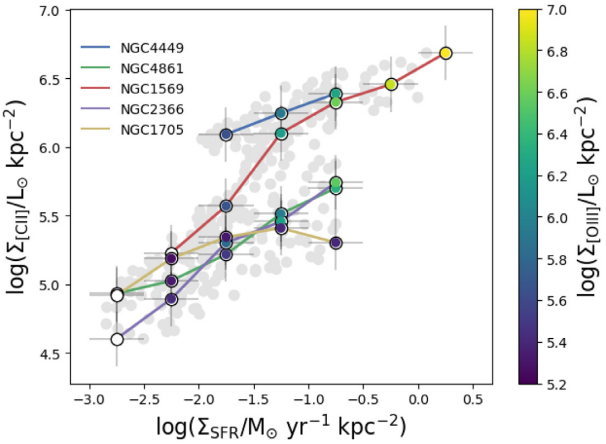

Figure A1. $\Sigma_{\rm [C\,II]}$ versus $\Sigma_{\rm SFR}$ relation in spatially resolved dwarf galaxies at $z = 0$: NGC 4449 (blue solid line), NGC 4861 (green), NGC 1509 (red), NGC 2366 (purple), and NGC 1705 (yellow). Data (in grey) are taken from De Looze et al. (2014) and aggregated in 0.5 dex wide $\Sigma_{\rm SFR}$ bins over which we compute the mean $\Sigma_{\rm [C\,II]}$. Points are colour-coded as a function of the mean $\Sigma_{\rm [O\,III]}$ value over the $\Sigma_{\rm SFR}$ bins. Those $\Sigma_{\rm SFR}$ bins for which the $\Sigma_{\rm [O\,III]}$ is undetected are shown in white.

APPENDIX B: THE POSTERIOR PROBABILITY DISTRIBUTIONS

In Fig. B1, we show for each galaxy/sub-component the corner plot of the 2D likelihood distributions for three parameters ($\kappa_{\rm s}$, Z, n) entering in our analytical models. Contours represent the 1σ, 2σ, and 3σ confidence levels.

Downloaded from https://academic.oup.com/mnras/article/505/4/5543/6296656 by Scuola Normale Superiore Biblioteca user on 14 November 2022

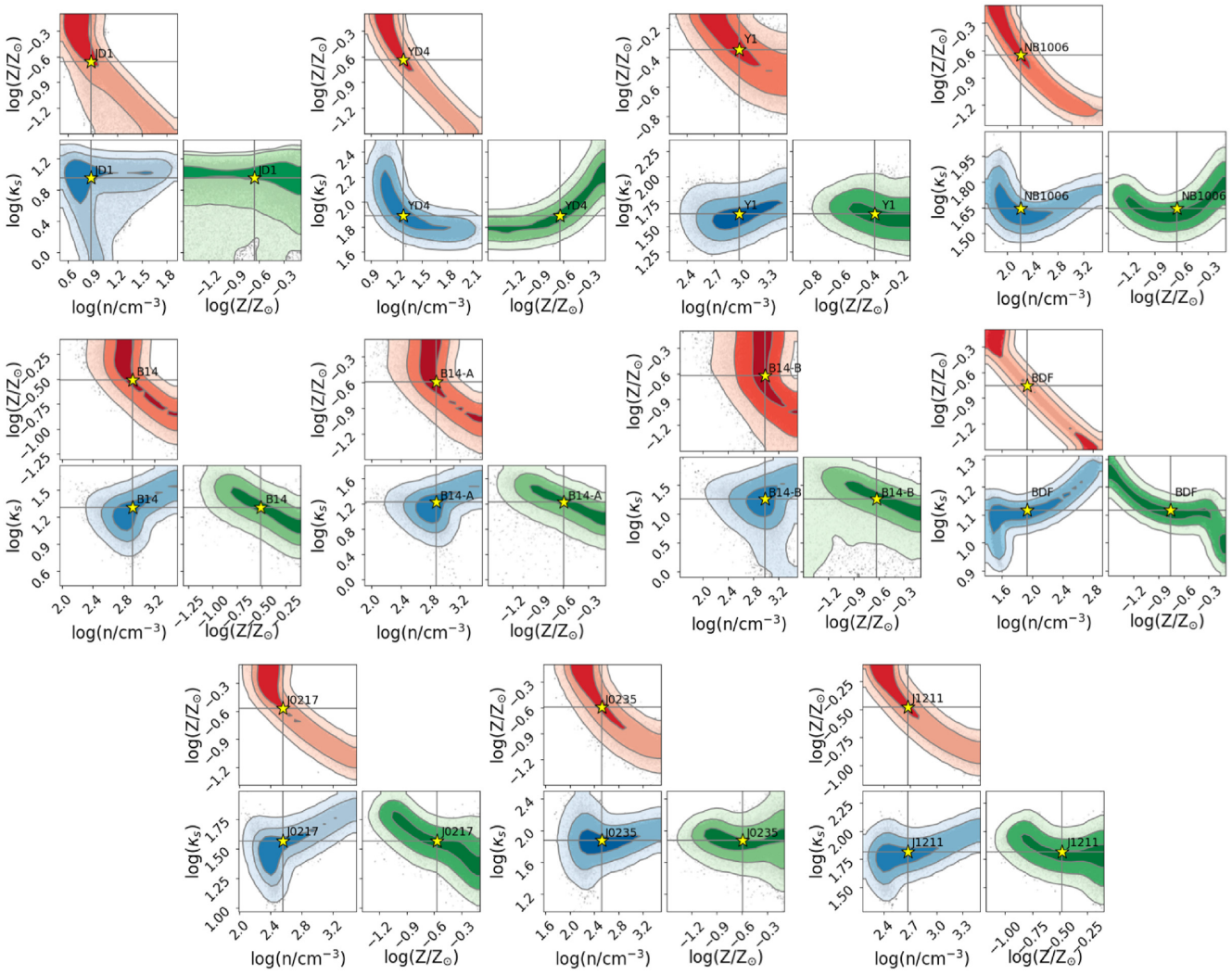

Figure B1. Corner plots with the results of the MCMC for all the galaxies analysed in this work. The name of each galaxy is indicated with a label close to the best-fitting location (yellow star) in each plot.

This paper has been typeset from a TEX/LATEX file prepared by the author.

Downloaded from https://academic.oup.com/mnras/article/505/4/5543/6296656 by Scuola Normale Superiore Biblioteca user on 14 November 2022